Time-of-Flight Flow Imaging Using NMR Remote Detection

J. Granwehr,* E. Harel, S. Han,† S. Garcia, and A. Pines

Materials Sciences Division, Lawrence Berkeley National Laboratory, and Department of Chemistry, University of California at Berkeley, Berkeley, California 94720-1460, USA

P. N. Sen and Y.-Q. Song‡

Schlumberger-Doll Research, 36 Old Quarry Road, Ridgefield, Connecticut 06877, USA

(Received 5 May 2005; published 10 August 2005)

A time-of-flight imaging technique is introduced to visualize fluid flow and dispersion through porous media using NMR. As the fluid flows through a sample, the nuclear spin magnetization is modulated by rf pulses and magnetic field gradients to encode the spatial coordinates of the fluid. When the fluid leaves the sample, its magnetization is recorded by a second rf coil. This scheme not only facilitates a time-dependent imaging of fluid flow, it also allows a separate optimization of encoding and detection subsystems to enhance overall sensitivity. The technique is demonstrated by imaging gas flow through a porous rock.

DOI: 10.1103/PhysRevLett.95.075503 PACS numbers: 61.43.Gt, 76.60.Pc, 83.85.Fg

NMR has become an invaluable tool for the characterization of materials owing to recent progress in instrumentation and experimental techniques [1]. In particular, the development of novel approaches to the control of spin coherence in the presence of inhomogeneous magnetic fields [2–4] and inside-out NMR hardware [5,6] highlight the potential of NMR in field studies of natural and industrial materials. For example, inside-out NMR was recently used to study methane-hydrate growth on the sea floor at a depth of 2500 m [7]. Furthermore, NMR has been recognized as a powerful method to visualize flow in porous media as evidenced in recent reports, e.g., Refs. [8–12].

One factor limiting the application of NMR for field experiments is that the sample is invariably outside the NMR instrument, causing a very poor filling factor and resulting in a low signal-to-noise ratio. This limitation can be overcome in some cases by performing the NMR experiment in two steps. Let us consider a fluid-filled porous object as an example. First, the spin manipulations by radio frequency (rf) radiation are performed on the fluid within the sample *in situ*, and then the spin magnetization is rotated onto the static magnetic field. After this (encoding) step, the fluid is removed from the sample into a highly optimized detection system to read out its longitudinal magnetization. As long as a substantial magnetic field exists along the flow path, the spin magnetization will follow the local field adiabatically, and no significant signal loss should occur en route to the detection system [13]. This idea of remote detection has been demonstrated recently to enhance the sensitivity of NMR spectroscopy and imaging [14,15].

A natural consequence of remote detection is that the received signal is dependent on the flow pattern in the sample. Fluid from the far end of the sample during encoding will arrive later than fluid nearer to the detector, and no signal will be detected from a stagnant region that is not effectively connected to the flow field. Heterogeneity in the flow field causes some flow paths to be preferred. This can be a result of the structural heterogeneity present in some porous samples like certain rocks, where it is believed to critically determine the crude oil recovery efficiency and rate. Most importantly, such heterogeneity might not be readily determined from a pore-level structural characterization, e.g., Refs. [16–20]. Using remote detection has the potential to overcome many technical difficulties in high field magnetic resonance imaging of rocks and to enable *in situ* studies of flow in the field. This Letter reports an experimental demonstration of flow imaging with remote detection by monitoring gas flow through a porous rock.

The basic idea of remote detection NMR is illustrated in Fig. 1(a), which highlights the fluid flowing through a porous object. The sample is placed within the active volume of the encoding coil, and a flow system is connected to transport the fluid downstream to the detection coil. An example of an rf pulse sequence is shown in Fig. 1(b). During the encoding step, an rf pulse is applied using the encoding coil in the presence of a magnetic field gradient to invert the spins only within a slice of the sample. The inverted spins then flow out of the sample into the detection coil, where a train of rf pulses is applied to detect a free induction decay signal after each pulse. The flow through the sample is characterized by the time-of-flight (TOF) of the fluid from the time of encoding to the time when it reaches the detector, allowing the entire TOF pattern to be recorded transiently.

Two independent rf probes were used for encoding and detection. Encoding was done using a commercial imaging probe (Varian Inc., Palo Alto, CA) with a cylindrical cavity along its full length. Detection was done with a homebuilt probe that could be inserted into the encoding probe. The coils of the two probes were placed close to each other in order to position both in the homogeneous region of the same magnet. The rf isolation between the two probes was achieved by a grounded copper shield. The NMR experi-

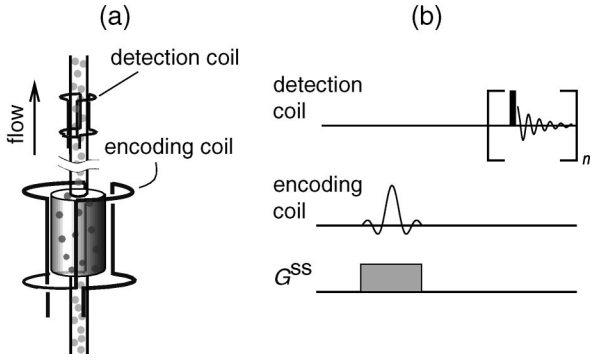

FIG. 1. Concept of remote detection NMR. (a) A porous sample (shaded cylinder) is placed in the active volume of the encoding coil. Information is encoded as polarization of the sensor medium (gray spheres), flowing out of the sample into the detection coil. A more field-capable setup could be designed especially for encoding, for example, by using a single-sided magnet and a surface rf coil [4–6]. (b) A pulse sequence for remote detection NMR. The encoding rf pulse in the presence of the field gradient G^{ss} is applied to invert the magnetization only in a slice perpendicular to the gradient direction. A train of n detection pulses is applied to measure the signal stroboscopically as the sensor medium gradually flows through the detection coil.

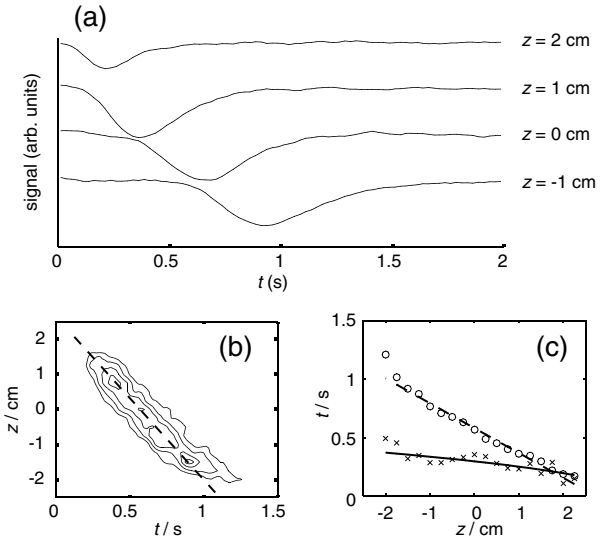

FIG. 2. Visualization of flow and dispersion through a rock sample. (a) TOF curves with slice-selective inversion of the spin magnetization along z. The position of the slice with respect to the center of the sample is indicated. The total gas pressure was 3 bar, and the flow rate was 0.55 slm. (b) Contour plot of the TOF curves with z sampled in steps of 2.5 mm. The pressure was 2.5 bar, and the flow rate was 0.50 slm. (c) Time of the minimum (○) and width of the dip (×) in the signal as a function of the position of the inverted slice. The data are the same as in (b). The dashed lines in (b) and (c) represent the mean velocity, and the full line in (c) is a fit of the dispersion of the gas inside the rock as described in the text.

ments were performed at 300 MHz on a Unity Inova spectrometer (Varian Inc.). The setup of the flow handling is detailed elsewhere [21].

The sample was a Bentheimer sandstone rock, 20 mm in diameter and 38 mm long, with a porosity of 22.5% and pore sizes of about 100 μm. It was inserted into a sealed plastic cocoon and connected to the flow setup using Teflon tubes. The flowing gas was a mixture of 1% Xe (natural abundance), 10% N_2, and 89% He. The ^{129}Xe nuclear spin polarization was optically enhanced [22,23] to about 10% using a XenoSpin polarizer (Amersham Health, Durham, NC). The gas flow rate was controlled between 0.4 and 0.8 slm (standard liter per minute) by two valves—one at the outlet of the polarizer and the other after the detection probe.

Figure 2(a) shows the TOF signal as a function of the time t between encoding and detection. For encoding, the ^{129}Xe magnetization was inverted in slices of 10 mm thickness perpendicular to the flow direction (z). The signal is constant before any encoded spins reach the detector. It drops as soon as inverted xenon arrives, and recovers to its maximum value once all the encoded gas has passed through the detector. For each trace, the field gradient was kept constant while the rf frequency was changed to select different slices. Since the slice at 2 cm is at the outlet of the sample, the inverted spins from that slice reach the detector significantly earlier than other slices closer to the sample inlet.

Figure 2(b) shows a contour plot of the TOF data of an identical experiment, but with slice thickness of 2.5 mm. The slope of this pattern represents the constant mean velocity of the gas flow in the rock, which was $v = 4.7$ cm/s as indicated by the line. The position of the minimum and the width of the dips of the TOF data are shown in Fig. 2(c). The time of the minimum shows an approximate linear dependence on z, indicative of the constant flow velocity. The width of the dip is broadened significantly for slices that are farther away from the detector. For these slices, the gas has traveled a longer distance to the detector compared to the slices near the exit. This broadening is due to hydrodynamic dispersion [24], with a contribution to the mean square displacement Δz^2 of approximately $2Kt$ at the long diffusion time limit. Taking into account the finite width Δz_0^2 at the sample outlet, we expect the width to grow for slices closer to the inlet as $\Delta z^2 \approx 2Kt + \Delta z_0^2$, which is indicated in Fig. 2(c) by the full line. Δz^2 was calculated from the time-domain full-width-at-half-height Δt as $\Delta z^2 = (v\Delta t)^2/8\ln(2)$. A dispersion coefficient $K \approx 0.3$ cm^2/s was obtained by fitting the data points from inside the rock, omitting points immediately after the inlet or before the outlet to avoid artifacts caused by the flow profile due to the inlet and outlet geometry. With a xenon diffusion constant $D_0 = 0.1$ cm^2/s in our gas mixture, dispersion due to diffusion [24] within the single pore channel alone cannot account for $K \sim 0.3$ cm^2/s in our sample [25]. It is likely that heterogeneity over multiple pore scales is responsible for this large K [26]. The large D_0 of xenon gas provides a unique opportunity to study dispersion at low Péclet numbers, which is a particularly

important regime to explore stagnant zones that upset the well-known theories for dispersion in porous media [27].

The inversion experiment discussed above does not resolve the two transverse dimensions. When the flow pattern is not uniform within the slice owing to, for instance, structural heterogeneity, it is desirable to image the flow in all three dimensions. Three-dimensional (3D) spatial encoding can be done in two ways. The first method achieves 3D imaging in a slice-by-slice fashion and acquires signals for many different slices by systematically scanning the rf frequency and the direction of the field gradient. This method is similar to the projection-reconstruction method introduced by Lauterbur [28].

A second method for 3D resolution uses phase encoding [15], as shown in Fig. 3(a). Magnetization is first rotated into the plane perpendicular to the applied magnetic field. Then a magnetic field gradient pulse is applied, which modulates the magnetization by a spatially dependent phase. One component of the precessing magnetization (either sine or cosine of the phase) is then stored along the applied field. Remaining transverse magnetization dephases quickly, while the sensor medium flows to the detector. Thus, only longitudinal magnetization survives the passage through the sample. All the Fourier components of the image can be sampled in this fashion by incrementing the gradient amplitude in all three dimensions.

This phase encoding approach works well if a full 3D image is to be acquired, which requires that field gradients along all three spatial dimensions be sampled independently. However, this point-by-point sampling of the spatial dimensions largely determines the total time of an experiment. By using a slice-selective preparation pulse, it is possible to encode a single slice in one dimension, while the other dimensions are imaged with phase encoding [Fig. 3(b)]. This reduces the number of phase encoding steps and, thus, the experimental time to obtain a 2D image. This is especially useful if the sample displays a certain symmetry and imaging the third dimension provides no additional information, for example, in case of cylindrical symmetry. The disadvantage is that slice-selective pulses can be considerably longer than hard pulses, which may effect a loss of signal for samples causing a short decoherence time of the flow medium in combination with rapid diffusion.

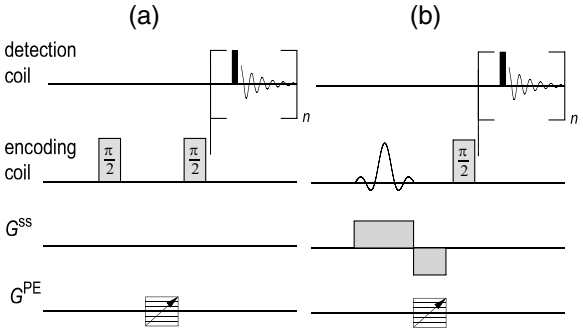

FIG. 3. Remote detection methods using phase encoding. (a) Gradient pulses in three directions, G^{PE}, provide 3D modulation of the spin magnetization. The second $\pi/2$ pulse stores the magnetization along the applied field. (b) Sequence for slice-selective phase encoding. The bipolar gradient G^{SS} is used for slice selection in one dimension, while phase encoding gradient pulses G^{PE} are used to resolve the other two spatial dimensions. In both methods, detection is done by a train of pulses whose spacing defines the time resolution of the TOF experiment.

Figure 4(a) shows three images of an experiment with full 3D phase encoding. These images reflect the encoding location of the gas molecules that arrive at the detector at times $t = 0.27$, 0.62, and 0.98 s after the encoding step. The leftmost image shows the gas near the exit and partly inside the narrow outlet region. The second image is centered approximately in the middle of the sample and further extended in the xy plane compared with the image at $t = 0.27$ s. The signal of the rightmost image is from the frontal region of the sample near the inlet. The gas distribution is radially uniform, indicating that the gas spreads uniformly into the entire cross section quickly after the inlet. The dips in the center of the images for $t = 0.62$ and 0.98 s are likely due to the flow characteristics in the exit region of the sample. The gas exiting the sample near the center experiences a significantly shorter path compared to the gas near the perimeter, while their respective longitudinal velocity is alike. As a result, for a given time to the

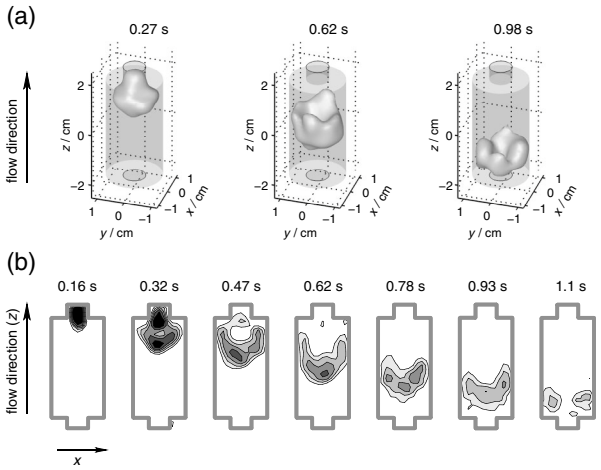

FIG. 4. Images of gas flow through the rock sample. The flow rate was 0.65 slm. The time between encoding and detection is indicated above each image. (a) A 3D representation of an isochronal surface at different times after the encoding step. The silhouettes represent the sample in its correct proportions, including the inlet and outlet. A 3D phase encoding sequence with hard encoding pulses was used. The total gas pressure was 3.7 bar. The resolution in all three dimensions was 0.46 cm. The experiment time was 36 min. (A movie of the complete data set is available for viewing [29].) (b) TOF x-z images with varying detection times after encoding. A slice of 0.75 cm thickness through the center of the rock was excited perpendicular to y, while x and z were resolved with 0.33 cm resolution using phase encoding. The pressure was 4.0 bar. The experiment time was 13 min.

detector, the gas in the center comes from a farther distance.

A series of 2D x-z images is shown in Fig. 4(b), obtained by selecting a slice perpendicular to y through the center of the sample, and with phase encoding along x and z. The times marked above the images are the detection time t after encoding, illustrating a time-resolved representation of the flow pattern. The reduction of the flow diameter is visualized near the exit ($t < 0.32$ s). The boomerang-shaped pattern for $t = 0.47$–0.93 s is a 2D representation of the dips in the 3D images discussed above for Fig. 4(a). The experiments were performed multiple times, and the 2D and 3D flow patterns were found to reproduce very well. Even in this type of rock, which has a high overall uniformity, small heterogeneities could be resolved, causing observable deviations of the flow pattern from the cylindrical symmetry of the sample.

An important factor in TOF experiments is the relative flow resolution, i.e., how many independent data points can be obtained from the pore volume V_p of the sample. Thus, a dimensionless flow resolution can be defined as

$$R = V_p/V_d, \tag{1}$$

where V_d is the detector volume. The experiments in Fig. 4 were done with $R \approx 15$. R can also be seen as a measure of how small the voxel size can be made while still resolving the dispersion of the sensor medium.

In conclusion, TOF NMR with remote detection represents a new way to characterize fluid flow through porous media. It combines the sensitivity advantage and increased flexibility of remote detection with the possibility to temporally resolve the flow field. Our experiments have demonstrated the feasibility of this approach, which may make it possible to study fluid flow in large, opaque samples. And finally, by using different sensor fluids of gas or liquid phases with varying pressures or flow rates, different regimes of dispersion can be explored experimentally, allowing further refinement of the understanding of flow in porous media.

The authors thank many for their help: D. Verganelakis for sample preparation, J. A. Seeley, M. P. Moschetti, and L. J. Chavez for experimental assistance, and M. D. Hürlimann for discussions. This work was supported by the Director, Office of Science, Office of Basic Energy Sciences, Materials Sciences and Nuclear Science Divisions, of the U.S. Department of Energy under Contract No. DE-AC03-76SF00098. E. H. is supported by the U.S. Department of Homeland Security under DOE Contract No. DE-AC05-00OR22750.

*Electronic address: joga@waugh.cchem.berkeley.edu
†Present address: Department of Chemistry and Biochemistry, University of California at Santa Barbara, Santa Barbara, CA 93106-9510, USA.
‡Electronic address: ysong@slb.com

[1] B. Blümich, *NMR Imaging of Materials* (Oxford University Press, Oxford, 2000).
[2] C. A. Meriles, D. Sakellariou, H. Heise, A. J. Moulé, and A. Pines, Science **293**, 82 (2001).
[3] T. M. Brill, S. Ryu, R. Gaylor, J. Jundt, D. D. Griffin, Y.-Q. Song, P. N. Sen, and M. D. Hürlimann, Science **297**, 369 (2002).
[4] J. Perlo, V. Demas, F. Casanova, C. A. Meriles, J. Reimer, A. Pines, and B. Blümich, Science **308**, 1279 (2005).
[5] R. L. Kleinberg and J. A. Jackson, Concepts Magn. Reson. **13**, 340 (2001).
[6] G. Eidmann, R. Savelsberg, P. Blümler, and B. Blümich, J. Magn. Reson., Ser. A **122**, 104 (1996).
[7] R. L. Kleinberg, C. Flaum, C. Straley, P. G. Brewer, G. E. Malby, E. T. Peltzer, G. Friederich, and J. P. Yesinowski, J. Geophys. Res. **108**, 2137 (2003).
[8] I. V. Koptyug, S. A. Altobelli, E. Fukushima, A. V. Matveev, and R. Z. Sagdeev, J. Magn. Reson. **147**, 36 (2000).
[9] S. Stapf, K. J. Packer, R. G. Graham, J.-F. Thovert, and P. M. Adler, Phys. Rev. E **58**, 6206 (1998).
[10] B. Manz, P. Alexander, and L. F. Gladden, Phys. Fluids **11**, 259 (1999).
[11] E. Kossel, M. Weber, and R. Kimmich, Solid State Nucl. Magn. Reson. **25**, 28 (2004).
[12] R. W. Mair, R. Wang, M. S. Rosen, D. Candela, D. G. Cory, and R. L. Walsworth, Magn. Reson. Imaging **21**, 287 (2003).
[13] A. Abragam, *Principles of Nuclear Magnetism* (Oxford University Press, Oxford, 1961).
[14] A. J. Moulé, M. M. Spence, S. Han, J. A. Seeley, K. L. Pierce, S. Saxena, and A. Pines, Proc. Natl. Acad. Sci. U.S.A. **100**, 9122 (2003).
[15] J. A. Seeley, S. Han, and A. Pines, J. Magn. Reson. **167**, 282 (2004).
[16] P. G. de Gennes, C. R. Acad. Sci. Ser. II **295**, 1061 (1982).
[17] M. H. Cohen and K. S. Mendelson, J. Appl. Phys. **53**, 1127 (1982).
[18] P. P. Mitra, P. N. Sen, L. M. Schwartz, and P. Le Doussal, Phys. Rev. Lett. **68**, 3555 (1992).
[19] Y.-Q. Song, S. Ryu, and P. N. Sen, Nature (London) **406**, 178 (2000).
[20] R. Wang, R. W. Mair, M. S. Rosen, D. G. Cory, and R. L. Walsworth, Phys. Rev. E **70**, 026312 (2004).
[21] S. Han, S. Garcia, T. J. Lowery, E. J. Ruiz, J. A. Seeley, L. Chavez, D. S. King, D. E. Wemmer, and A. Pines, Anal. Chem. **77**, 4008 (2005).
[22] T. G. Walker and W. Happer, Rev. Mod. Phys. **69**, 629 (1997).
[23] B. M. Goodson, J. Magn. Reson. **155**, 157 (2002).
[24] G. I. Taylor, Proc. R. Soc. A **219**, 186 (1953).
[25] M. D. Hürlimann, K. G. Helmer, L. L. Latour, and C. H. Sotak, J. Magn. Reson., Ser. A **111**, 169 (1994).
[26] R. Duplay and P. N. Sen, Phys. Rev. E **70**, 066309 (2004).
[27] P. G. de Gennes, J. Fluid Mech. **136**, 189 (1983).
[28] P. C. Lauterbur, Nature (London) **242**, 190 (1973).
[29] See EPAPS Document No. E-PRLTAO-95-067533 for a movie showing the full TOF data of gas flowing through the rock sample. This document can be reached via a direct link in the online article's HTML reference section or via the EPAPS homepage (http://www.aip.org/pubservs/epaps.html).